JACS
JOURNAL OF THE AMERICAN CHEMICAL SOCIETY

Article

pubs.acs.org/JACS

In Situ Anomalous Small-Angle X-ray Scattering Studies of Platinum Nanoparticle Fuel Cell Electrocatalyst Degradation

James A. Gilbert,*[,†] Nancy N. Kariuki,[‡] Ram Subbaraman,[‡] A. Jeremy Kropf,[‡] Matt C. Smith,[‡] Edward F. Holby,[†,§] Dane Morgan,[†] and Deborah J. Myers[‡]

[†]Department of Materials Science and Engineering, University of Wisconsin—Madison, Madison, Wisconsin 53706, United States
[‡]Chemical Sciences and Engineering Division, Argonne National Laboratory, Lemont, Illinois 60439, United States

Supporting Information

ABSTRACT: Polymer electrolyte fuel cells (PEFCs) are a promising high-efficiency energy conversion technology, but their cost-effective implementation, especially for automotive power, has been hindered by degradation of the electrochemically active surface area (ECA) of the Pt nanoparticle electrocatalysts. While numerous studies using ex situ post-mortem techniques have provided insight into the effect of operating conditions on ECA loss, the governing mechanisms and underlying processes are not fully understood. Toward the goal of elucidating the electrocatalyst degradation mechanisms, we have followed Pt nanoparticle growth during potential cycling of the electrocatalyst in an aqueous acidic environment using in situ anomalous small-angle X-ray scattering (ASAXS).

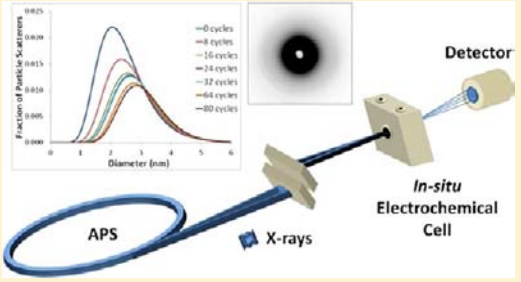

ASAXS patterns were analyzed to obtain particle size distributions (PSDs) of the Pt nanoparticle electrocatalysts at periodic intervals during the potential cycling. Oxide coverages reached under the applied potential cycling protocols were both calculated and determined experimentally. Changes in the PSD, mean diameter, and geometric surface area identify the mechanism behind Pt nanoparticle coarsening in an aqueous environment. Over the first 80 potential cycles, the dominant Pt surface area loss mechanism when cycling to 1.0−1.1 V was found to be preferential dissolution or loss of the smallest particles with varying extents of reprecipitation of the dissolved species onto existing particles, resulting in particle growth, depending on potential profile. Correlation of ASAXS-determined particle growth with both calculated and voltammetrically determined oxide coverages demonstrates that the oxide coverage is playing a key role in the dissolution process and in the corresponding growth of the mean Pt nanoparticle size and loss of ECA. This understanding potentially reduces the complex changes in PSD and ECA resulting from various voltage profiles to a response dependent on oxide coverage.

INTRODUCTION

Polymer electrolyte fuel cells (PEFCs) show promise as a high-efficiency energy conversion technology for both mobile and stationary power applications. The main attraction of this technology is the increase in energy efficiency through the direct conversion of chemical energy to electrical energy via the oxidation of hydrogen and reduction of oxygen to form water. Electrocatalysts are required to enhance the kinetics of both the hydrogen oxidation (anode) and oxygen reduction (cathode) reactions. These electrocatalysts are typically Pt or Pt alloy nanoparticles supported on high surface area carbon (Pt/C). Pt-containing electrocatalysts are preferred due to their high activity and relative stability in the acidic environment of the PEFC.[1,2]

A major challenge to cost-effective implementation of PEFC technology in a wide range of applications is sustaining the power output over the desired lifetime of the device. The major contributing factor to the diminishing output is the loss of electrochemically active surface area (ECA) of the cathode electrocatalyst.[3,4] Ex situ transmission electron microscopy (TEM) and X-ray diffraction (XRD) analyses of PEFC cathode catalyst layers after long-term steady-state and potential cycling operation have revealed possible sources of ECA loss: dramatic coarsening of the platinum or platinum alloy particles and loss of platinum into electrochemically inaccessible regions of the membrane electrode assembly (MEA), such as into the membrane electrolyte.[3,5−11] There are several mechanisms proposed for loss of ECA.[4,12,13] These include dissolution of Pt from smaller particles and redeposition of the soluble Pt species onto larger particles on the carbon support. This mechanism is termed "electrochemical Ostwald ripening" and is driven by the difference in thermodynamic stability of particles of different diameter.[12] Another proposed mechanism is diffusion of the Pt ions into the membrane, creating large crystallites through reduction by crossover hydrogen. A third proposed mechanism of ECA loss is through coalescence of Pt particles via migration on the carbon support surface. The last mechanism involves Pt particle agglomeration and may be enhanced by corrosion of the carbon support.

Much has been learned about the mechanisms and factors influencing catalyst ECA loss from in situ ECA measurements

Received: April 20, 2012
Published: August 2, 2012

   dx.doi.org/10.1021/ja3038257 | J. Am. Chem. Soc. 2012, 134, 14823−14833

and from ex situ, post-mortem analyses using scanning electron microscopy and energy-dispersive X-ray analysis to determine platinum distribution and TEM and XRD to determine catalyst particle size distributions (PSDs). The predominance and rates of the three proposed mechanisms appear to depend on cell conditions, most notably the cell voltage and cycling protocol. Pt is lost from the cathode and deposits in the membrane, with the extent of loss and the amount of Pt found in the membrane increasing with the upper voltage limit of cycling.[4,7,13−18] The Pt particles remaining in the electrode have altered size distributions (e.g., 2−3 nm to ∼10 nm after 10 000 cycles between 0.6 and 1.0 V), with greater particle size growth and ECA loss noted when cycling between potential regions where Pt is oxidized and reduced as compared to potentiostatic conditions.[3,7,19−22] In addition, the rates and extent of these changes increase with anodic potential limit[7,8,23] and anodic sweep rate.[20,21] The potential dependence of Pt dissolution is often invoked as the source of the observed potential dependence of ECA loss rates, particle growth, and Pt loss into the membrane.[8,13,23−27] Aqueous electrolyte experiments showing increased rates of Pt dissolution with increasing anodic potential limit for polycrystalline Pt[28,29] and for Pt/C[30] support this argument.

While these ex situ studies provide valuable information on catalyst degradation and the effect of operating conditions, the post-mortem nature of the diagnostic techniques used limits the correlation of evolution of the size distribution and number of electrocatalyst particles at each diameter with time and conditions. Such information is critical for determining the intrinsic effect of particle diameter on stability and for correlating stability with loss of ECA. Such information can define conditions to mitigate ECA loss, extend catalyst activity lifetime, and aid in the design of more durable and economically viable electrocatalysts.

The aim of this study was to investigate the influence of potential profile (i.e., shape and anodic potential limits) on Pt particle growth through in situ determination of PSDs during potential cycling and under potential hold conditions in an aqueous acidic electrolyte. The in situ measurements were performed using anomalous small-angle X-ray scattering (ASAXS). The oxide coverages attained during the profiles were determined using cyclic voltammetry and were also calculated using theoretical modeling. These coverages have been correlated with particle growth, determined using ASAXS, and with extent of loss of Pt into the electrolyte, determined using inductively coupled plasma−mass spectrometry. In these studies, an aqueous acidic environment using nonadsorbing perchloric acid electrolyte was used to model the PEFC environment. While there are many differences between the aqueous and PEFC environments, as discussed elsewhere,[27,31] the aqueous environment offers the clear advantage of allowing determination of the loss rates of Pt from the electrode by analytical measurement of Pt concentration in the electrolyte. In addition, aqueous electrolyte, rotating disk and rotating ring−disk measurements are typically used to screen the activity and durability of newly developed electrocatalysts.[2,32]

Unlike TEM, the common technique used for determining Pt/C PSDs,[3,5,7,12,13,33] ASAXS is an in situ technique, as X-rays can be tuned to penetrate through surrounding low atomic number materials. This enables correlation of ECA loss with changes in PSDs induced by processes associated with the change in potential and potential profile. ASAXS also provides the absolute number of particles within the area exposed to the incident X-ray beam (approximately 1 mm^2), probing billions of particles for typical catalyst loadings (0.1−0.4 mg Pt/cm^2). However, TEM images are essential for determining the shape of the particles, which is used to select the correct scattering form factor for ASAXS data analysis.

As an introduction, we will briefly discuss the theory behind ASAXS. In-depth discussions of ASAXS theory can be found in several textbooks and publications.[34−38] Small-angle X-ray scattering (SAXS) is a well-established technique for probing particle sizes and distributions on the nanometer level.[39] In SAXS, the scattered X-ray intensity is measured as a function of the scattering vector, Q, which is proportional to the scattering angle. SAXS, however, does not provide element specific results but rather a combination of the scattering patterns of all the elements found in the beam path. To obtain the specific SAXS spectrum of the desired element, one needs to prepare and analyze an equivalent sample without the element of choice then subtract out the scattering due to this background sample (i.e., background subtraction). This is difficult to do for complex systems (i.e., ones with many elements), but it has been implemented and been proven to work on simpler systems.[33,40]

On more complex systems, ASAXS proves to be an easier method than SAXS for obtaining element specific results. In ASAXS, SAXS intensities are measured at several X-ray energy levels (E) preceding the absorption edge energy of the element of interest. For the subject of this study, Pt nanoparticles supported on porous carbon (Pt/C), the measured SAXS intensity is given by

$$I_M(Q, E) = I_{Pt}(Q, E) + I_C(Q, E) \quad (1)$$

where $I_{Pt}(Q,E)$ and $I_C(Q,E)$ are the SAXS intensities resulting from the Pt and the carbon support, respectively. Near the absorption edge, these intensities and the atomic form factor, also known as the scattering factor, are strongly correlated to the X-ray energy. The atomic form factor of the Pt dips sharply near the Pt-L_3 absorption edge, as shown in Figure 1a, while the form factor of the carbon remains unchanged. This difference between the scattering factor of the Pt and C is known as the scattering contrast and, as illustrated in Figure 1a, is dependent on the energy of the incoming X-ray beam. Once the scattering contrast of the system is known for chosen energies, the ASAXS spectra at these energies can be analyzed simultaneously to obtain the PSD of the Pt nanoparticles, as illustrated in Figure 1b.

Previous studies using SAXS and ASAXS on Pt/C electrodes have been reported by Haubold et al.,[34,41] Smith et al.,[33] and Yu et al.[42] Haubold et al. and Smith et al. reported reversible Pt particle growth attributed to oxide formation. Haubold et al. reported a 1 nm reversible growth, attributed to oxide formation, when comparing Pt particle diameters at 1.32 versus 0.47 V. Smith et al. reported similar reversible particle growth during potential cycling up to 1.4 V and irreversible particle growth resulting from the potential cycling. Yu et al. showed that smaller initial mean particle sized catalysts (2−3 nm) were less stable than larger initial mean sized catalysts (>5 nm) when cycled up to 1.16 V.

EXPERIMENTAL SECTION

Preparation of Electrodes. Commercial carbon-supported platinum (20 wt % Pt on XC-72 Vulcan carbon, E-Tek) electrocatalyst powder was mixed with an appropriate amount of perfluorosulfonic acid binder (5 wt % Nafion, Sigma-Aldrich, in a mixture of lower

dx.doi.org/10.1021/ja3038257 | J. Am. Chem. Soc. 2012, 134, 14823−14833

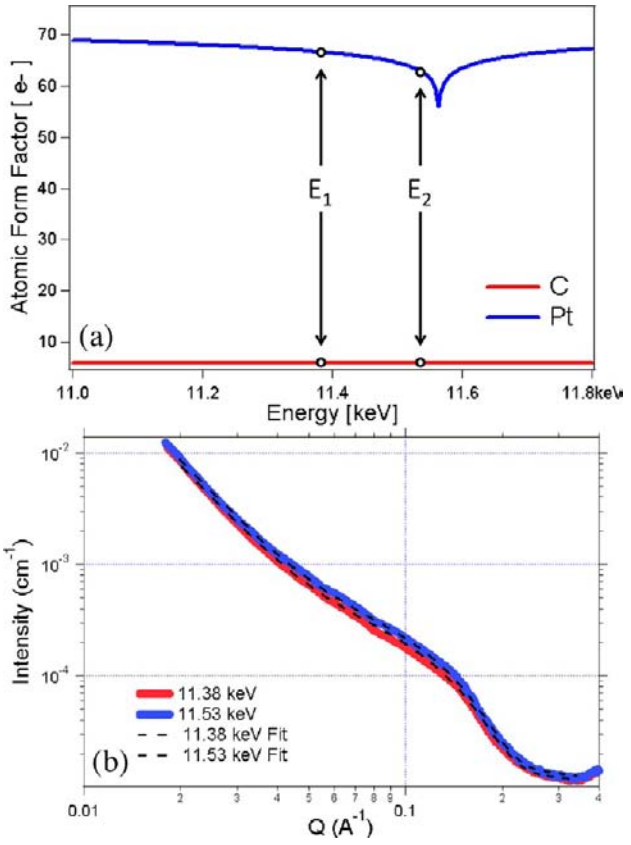

Figure 1. (a) Atomic form factor as a function of energy near the Pt-L_3 absorption edge for Pt (blue) and C (red). E_1 and E_2 are two of the energy levels where measurements were recorded and analyzed on the basis of scattering contrast. (b) Example of averaged ASAXS data at E_1 = 11.38 keV and E_2 = 11.53 keV along with their respective log-normal fits.

aliphatic alcohol and water) diluted with methanol to result in a catalyst to dry Nafion volume ratio of 1:1. The suspension was deposited onto 126 μm thick grafoil sheets (Strem) as a circle with geometric area of 0.69 cm^2 and a platinum loading of 0.4 mg/cm^2.

Electrochemical Setup. The Pt/C/Nafion samples served as the working electrode and were immersed in a 0.1 M perchloric acid electrolyte (GFS, double distilled, in 18 MΩ Millipore water) contained in a PTFE electrochemical cell specially designed for in situ X-ray absorption and scattering measurements of nanoparticle electrocatalysts. The cell has been described previously (Myers et al., Figure 1b).[31] The cell has an electrolyte cavity volume of 10 mL with an attached PTFE spacer in the center of the cavity to minimize the X-ray pathway through the electrolyte (X-ray path length of 3.5 mm). The spacer has a hole in its center, for transmission of X-rays, which is sealed with Kapton tape to contain the electrolyte. The grafoil working electrode also sealed the electrolyte cavity and was supported by an aluminum faceplate with a circular cutout to allow transmission of the X-ray beam. Two holes at the top of the cell were used to immerse the counter and reference electrodes into the electrolyte. The counter electrode was carbon cloth, to avoid introduction of Pt or other precious metals into the aqueous system, and the reference electrode was either Ag/AgCl or Hg/Hg_2SO_4 (0.5 M H_2SO_4 filling solution). Throughout this paper, all potentials are referenced to the reversible hydrogen electrode (RHE). Potentials were controlled using CH Instruments models 660B and 760C potentiostats.

Preconditioning of the electrodes before the X-ray experiments was performed by cycling the potential of the working electrodes between the open circuit potential to the hydrogen evolution region. Typically the electrodes were subjected to only a few of these preconditioning cycles to remove adsorbed impurities from the Pt surfaces.

Four potential profiles were utilized in this work through a total of seven experiments: potentiostatic, triangle, trapezoid, and square (Figure 2). All experiments along with the preconditioning of the

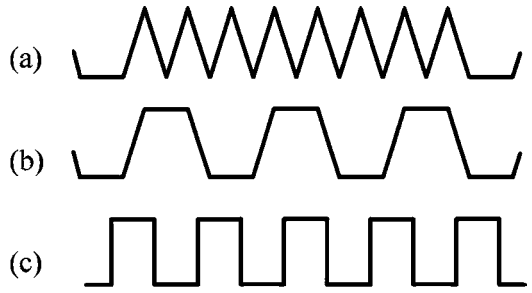

Figure 2. Illustration of the three potential cycling profiles studied: (a) triangle, (b) trapezoid, and (c) square. ASAXS data was recorded during potential holds at 0.4 V.

electrodes were performed at room temperature (21 °C). Two potentiostatic experiments were performed: 1.0 V for 16 h and 1.1 V for 24 h. Two experiments utilized a 10 mV/s triangle potential profile with cathodic potential limit of 0.4 V and anodic potential limits of 1.0 or 1.1 V. The cycling was periodically stopped and the cell was held at a potential of 0.4 V while the ASAXS data were collected. Two experiments utilized a trapezoid potential profile with 10 mV/s sweeps between 0.4 V and either 1.0 or 1.1 V with 240 s holds at each limit. A seventh experiment utilized a square wave potential profile with 140 s potential holds at 0.4 and 1.1 V. In order to obtain the irreversible growth attributed to coarsening of the Pt only, the ASAXS data in this study was obtained while potentiostating the electrodes at 0.4 V, a potential at which Pt nanoparticles have been reported to be oxide-free.[43,44]

A summary of the experimental parameters and conditions is given in Table 1. The seven experiments will be referenced throughout the paper as: static-1.0, static-1.1, triangle-1.0, triangle-1.1, trapezoid-1.0, trapezoid-1.1, and square-1.1.

Table 1. Overview of Experimental Conditions Used in Each Experiment and Reference Names Used Throughout the Paper

experiment reference name	cathodic potential limit (V)	anodic potential limit (V)	sweep rate (mV/s)	time of constant potential hold (per cycle)
static-1.0	–	1.0	–	16 h
static-1.1	–	1.1	–	24 h
triangle-1.0	0.4	1.0	10	0 s
triangle-1.1	0.4	1.1	10	0 s
trapezoid-1.0	0.4	1.0	10	240 s
trapezoid-1.1	0.4	1.1	10	240 s
square-1.1	0.4	1.1	–	140 s

Scattering Experiment and Data Analysis. ASAXS measurements were performed at the Advanced Photon Source at Argonne National Laboratory (Argonne, IL) at the bending magnet beamline 12-BM. Scattering patterns were recorded for all samples over 5-s intervals at eight different energy levels near the Pt-L_3 X-ray absorption edge (11.564 keV) over a scattering vector range of 0.017−0.61 $Å^{-1}$ using a MAR CCD detector. The scattering vector is the difference between the incoming X-ray wave vector and the scattered X-ray wave vector. The scattering wave vector is equal to $4\pi \sin \theta/\lambda$, where 2θ is the scattering angle and λ is the X-ray wavelength. Beam spot size was approximately 0.01 cm^2. An example of the small-angle X-ray scattering profiles for the Pt/C/Nafion at two of the X-ray energy levels is shown in Figure 1b. This figure is a log−log plot of the X-ray scattering intensity versus the scattering vector, Q, and shows that the scattering intensity increases as the scattering vector decreases. The

dx.doi.org/10.1021/ja3038257 | J. Am. Chem. Soc. 2012, 134, 14823−14833

two solid lines represent the scattering waves at two energy levels near the Pt-L_3 edge: E_1 = 11.38 keV and E_2 = 11.53 keV. The PSDs shown in this paper were determined by fitting the scattering profiles obtained at three or more energy levels.

The ASAXS data analysis was carried out using the Modeling II macro of Irena, a suite of macros written specifically for SAXS data analysis for Igor Pro 6 software.[45,46] Modeling II allows simultaneous fitting of multiple particle populations and does not assume a set mathematical function for the distributions. In all samples studied here, the particle size distributions obtained from Modeling II could be fit with a log-normal function. Previous TEM and XRD studies on carbon-supported Pt nanoparticles also found that Pt/C distributions are best fit by a log-normal function.[8,45,48] The Pt scattering data were therefore fit using a log-normal distribution in the range 0.02 $Å^{-1} < Q < 0.35$ $Å^{-1}$, assuming the Pt particles are spheres, polydispersed, and scatter independently (i.e., approximated as a dilute system in Irena fitting).[47,49] This range of scattering vector (Q) corresponds to a diameter range of approximately 1.8−6.3 nm. The scattering intensity in this range results from primary platinum particles and not from cluster scattering.[50]

The overlying dashed lines in Figure 1b are the Irena log-normal fits to the ASAXS data. The log-normal function is given by the equation:

$$f(r) = \frac{1}{\sqrt{2\pi}\sigma r}\exp\left(-\frac{(\ln r - \mu)^2}{2\sigma^2}\right) \quad (2)$$

where r is the particle radius, σ is the standard deviation, and μ is the mean particle size. Compared to a Gaussian, the log-normal function is skewed toward larger particle sizes as the standard deviation increases and is more Gaussian-like as it decreases.

Post-mortem Characterization. After the cycling experiments, the Pt PSDs were further analyzed using TEM. Samples were prepared by scraping the cycled catalysts off the grafoil and dispersing them in 2-propanol to form dilute suspensions. The suspensions were drop-cast onto carbon-coated copper grids followed by solvent evaporation in air at room temperature. Images were taken using a Philips CM30T transmission electron microscope at an accelerating voltage of 200 kV at the Electron Microscopy Center at Argonne National Laboratory. The size distribution of the Pt nanoparticles was obtained by directly measuring the size of at least 200 randomly chosen particles in the TEM images. The ex situ PSDs from TEM were compared to the pre- and postcycling ASAXS-derived distributions.

Determination of Amount of Dissolved Pt. To elucidate the influence of Pt dissolution on the changes in mean particle size with potential cycling, five electrodes were subjected to 160 cycles of the five different potential cycle protocols shown in Table 1. After cycling, the concentration of dissolved Pt in the electrolyte was determined using high-resolution inductively coupled plasma-mass spectrometry (Fisons Quadrupole PQII+ ICPMS and VG Elemental High-Resolution AXIOM ICP-MS) with a Pt detection limit of 1 ppt. ICP-MS-determined dissolved Pt concentrations have been shown to accurately reflect mass loss from a Pt electrode determined using an electrochemical quartz crystal nanobalance.[54] The Pt concentration in the electrolyte prepared from as-received perchloric acid and Millipore water was determined to be 12 ppt (6.2×10^{-11} M). The fractions of the initial Pt loadings dissolved from the electrode as a result of the 160 cycles were calculated using the initial Pt loading (0.28 mg), the ICP-MS-determined dissolved Pt concentrations, and the electrolyte volume (9 mL).

Measurement and Calculation of Oxide Coverage. Gas diffusion electrodes containing the Pt/C catalyst (E-Tek) were coated with Nafion solution (5 wt % in aliphatic alcohols and water, Aldrich) to form an ionomer loading of 0.2 mg/cm^2 (dry basis). The samples were dried overnight at 60 °C and then soaked in deionized water for at least 3 days. Small pieces (~4 × 4 mm^2) were cut from a larger piece and a gold wire (0.25 mm diameter) was wrapped around each piece to make electrical contact with the Pt/C. The Nafion-coated gas diffusion electrodes were immersed in 0.1 M $HClO_4$ electrolyte and tested in a standard glass three-electrode electrochemical cell. Gold counter electrodes were isolated in a separate fritted compartment. The reference electrode was Hg/Hg_2SO_4 with 0.5 M H_2SO_4 filling solution. All potentials are reported vs the RHE scale.

The Pt/C electrodes were pretreated by cycling (~30 cycles between 0.03 and 1.1 V) at various scan rates (decreasing from 100 to 5 mV/s). The charge corresponding to the adsorbed hydrogen (H_{upd}) (between potentials of 0.05 and 0.5 V) was used to calculate the Pt ECA using an area-specific charge of 210 $\mu C/cm^2$. The high scan rate voltammograms were also used to calculate the charge associated with the pseudocapacitive carbon redox couple positioned between 0.6 and 0.7 V in the anodic scan. This charge was subtracted from the oxide reduction charges to determine the oxide coverages attained during the potential scan/hold experiments. Samples of relatively similar ECA (±5−6%) were used for all studies.

Oxide coverages were determined for two potential cycling profiles: triangular wave from 0.4 V to either 1.0 or 1.1 V followed by a cathodic sweep to 0.05 V at scan rates ranging from 1 mV/s to 10 mV/s and trapezoidal wave with potentials ramped at the same scan rate as the previous case, followed by a hold at the upper limit for a time of 30−300 s followed by the return sweep to 0.05 V. The cathodic sweep was used to estimate the coverage of oxide after accounting for the H_{upd} and the carbon redox pseudocapacitance charges. The reported oxide coverages assume $2e^-$ flow for each oxygen atom binding to the surface where one monolayer of oxide is equivalent to two times the H_{upd} charge.

Theoretical oxide coverages for the various profiles were calculated using a thermokinetic model described in detail by Holby et al.[27,52]

RESULTS AND DISCUSSION

Transmission Electron Microscopy. TEM images of the catalyst before and after the various cycling protocols are shown in Figure 3. Though a few irregularly shaped particles or agglomerates of particles are evident, the majority of particles are spherical. The Pt particles were thus treated and fit as polydisperse spheres with aspect ratios of 1 for the ASAXS data analysis. Assumption of other form factors and aspect ratios (e.g., cylinders or rods) for the ASAXS fitting resulted in unrealistic particle sizes as compared to the TEM-determined particle sizes. There was no evidence of major carbon corrosion in the postcycling TEM images for any of the experiments.

Mean Pt Particle Diameter. The results of the number mean particle diameter as a function of time, as determined from the ASAXS analysis, for the triangle-1.0, trapezoid-1.0, and static-1.0 electrodes are shown in Figure 4a. The results for the triangle-1.1, trapezoid-1.1, square-1.1, and static-1.1 electrodes are shown in Figure 4b. The initial Pt mean particle diameter for all the samples, as determined from the ASAXS analysis, was found to be approximately 2.25 nm. The initial mean diameter from TEM analysis was 2.7 ± 0.7 nm.

A summary of initial and final mean particle sizes for all of the electrodes is shown in Table 2. The electrodes subjected to potentiostatic holds, static-1.0 and static-1.1, showed significantly less growth of the mean particle diameter than the electrodes subjected to potential cycling. The mean Pt particle size of the electrodes subjected to potentiostatic holds for 16 and 24 h, static-1.0 and static-1.1, increased only 0.04 and 0.06 nm, respectively. These increases in mean particle diameter are within the error of the measured values and thus no significant growth was observed over the duration of the measurements.

Significant Pt particle growth was observed for the electrodes subjected to potential cycling profiles. Growth in the mean Pt particle size was found to be on the order of tenths of a nanometer for the cycled electrodes as compared to less than a tenth of a nanometer for the potentiostated electrodes. A comparison of the change in mean particle size as a function of the number of potential cycles for the five different cycling

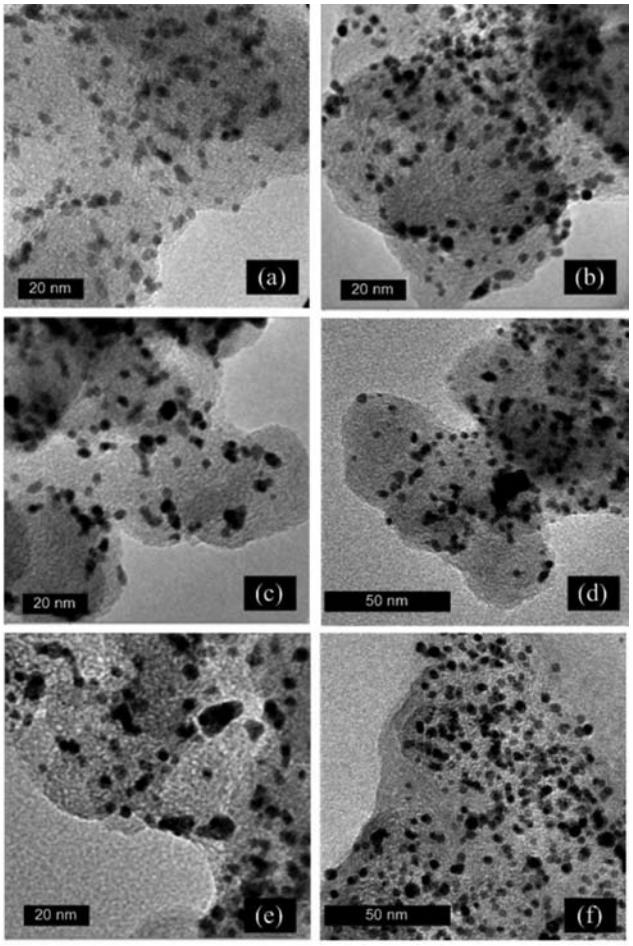

Figure 3. Sample TEM images for the (a) initial catalyst, (b) triangle-1.0, (c) trapezoid-1.0, (d) triangle-1.1, (e) trapezoid-1.1, and (f) square-1.1, used to determine post-mortem ex situ PSDs.

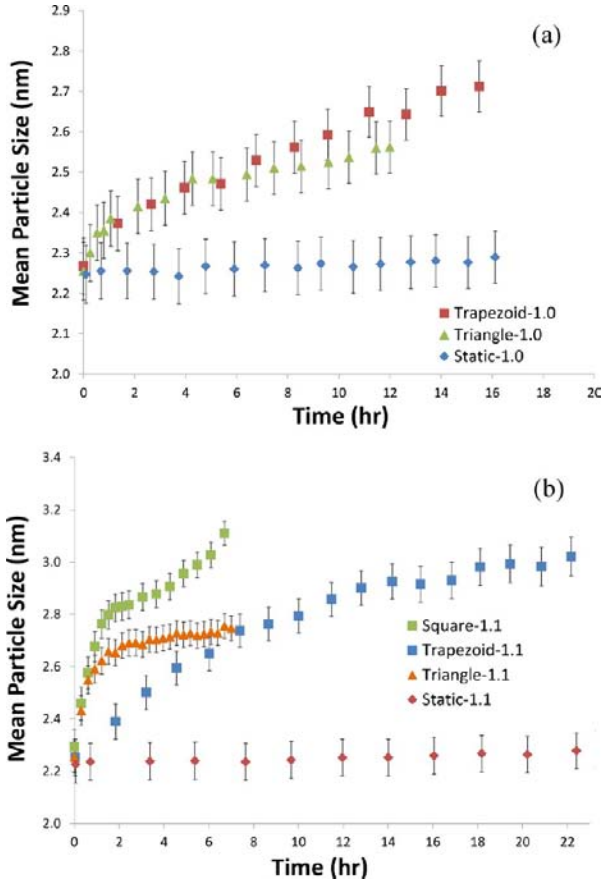

Figure 4. Mean particle size growth of Pt/C electrocatalysts over the duration of the experiments for experiments with anodic potential limits of (a) 1.0 V and (b) 1.1 V.

protocols is shown in Figure 5. This plot illustrates that the type of profile has a pronounced effect on the growth in mean particle size, with the square wave inducing more particle growth than the trapezoidal wave and the trapezoidal wave inducing more particle growth than the triangle wave. Figure 5 also demonstrates that the anodic limit of 1.1 V causes a larger growth in mean particle size than the 1.0 V anodic limit.

Figure 5b shows a region over which the mean particle size is relatively invariant with increasing number of cycles for all three profiles. This "plateau" region is the most pronounced and of the longest duration for triangle-1.1 (>50 cycles at 2.7−2.75 nm) and more pronounced for square-1.1 (24−48 cycles at 2.8 to 2.9 nm) than for trapezoid-1.1 (70−94 cycles at 2.8−2.9 nm). This type of plateau was also seen by Smith et al. for Pt particles subjected to a potential step profile up to 1.4 V, with the plateau occurring at approximately 3.2 nm.[33] Such a plateau region may indicate that the catalyst has reached a stable or quasistable state or particle size distribution. A similar increase in growth rate after a period of slower growth has also been observed by Yu et al.[42] They speculated that the catalyst entered into a second accelerated growth stage, the cause of which could not be explained from the experimental results.

The post-mortem mean diameters as determined by TEM are compared with the terminal ASAXS-determined mean diameters in Table 2. This comparison shows that the TEM-determined mean diameters are consistently higher than the ASAXS-determined mean diameters, though the ASAXS diameters do fall within the error bars of the TEM measurements. The differences between ASAXS- and TEM-determined mean diameters can be attributed to the small sample size counted in the TEM analysis, resulting in much larger error values (<0.1 nm for ASAXS and >0.5 nm for TEM), and the under-representation of small particles in the TEM distributions due to the difficulty of resolving particles of <1 nm diameter in the TEM images.[45] Comparisons between SAXS and TEM PSDs have been previously reported for similar systems.[53,54]

Particle Size Distributions. Particle size distributions were derived from the log-normal fitting of the ASAXS data. In situ PSDs at periodic intervals, up to ∼80 potential cycles, for the five different potential cycling protocols are shown in Figure 6. The initial distributions, labeled "0 cycles", are those obtained immediately following the preconditioning cycles and before any long-term potential cycling was initiated. Normalized initial distributions (Figure 6a) were found to be similar in width with only the triangle-1.1 having a slightly narrower distribution. The PSD obtained from TEM analysis, also shown in Figure 6a, shows good agreement with the ASAXS-derived PSDs.

As shown in Figure 6b−f, the general trend for evolution of the PSD with potential cycling for all the cycling protocols is a loss of smaller particles, less than ∼3 nm in diameter, and an increase in the number of larger particles, greater than ∼3 nm in diameter. The impact of the first 80 cycles of each profile on the number of small and large particles, as represented by 1.50

dx.doi.org/10.1021/ja3038257 | J. Am. Chem. Soc. 2012, 134, 14823−14833

Table 2. Summary of Experimental Conditions, ASAXS Results, and Post-mortem TEM Results

experiment reference name	total cycles	initial mean particle size (nm)	final mean particle size (nm)	overall particle growth (nm)	final mean particle size from TEM (nm)
triangle-1.0	360	2.26 ± 0.07	2.56 ± 0.06	0.31 ± 0.10	2.9 ± 1.1
trapezoid-1.0	81	2.27 ± 0.07	2.71 ± 0.06	0.44 ± 0.10	3.2 ± 0.8
triangle-1.1	181	2.25 ± 0.06	2.75 ± 0.05	0.49 ± 0.10	3.0 ± 0.6
trapezoid-1.1	132	2.25 ± 0.07	3.07 ± 0.08	0.81 ± 0.10	3.5 ± 1.4
square-1.1	88	2.29 ± 0.07	3.11 ± 0.05	0.82 ± 0.08	3.0 ± 0.7
static-1.0	–	2.25 ± 0.07	2.29 ± 0.07	0.04 ± 0.10	2.4 ± 0.8
static-1.1	–	2.23 ± 0.07	2.29 ± 0.07	0.06 ± 0.10	2.5 ± 0.8

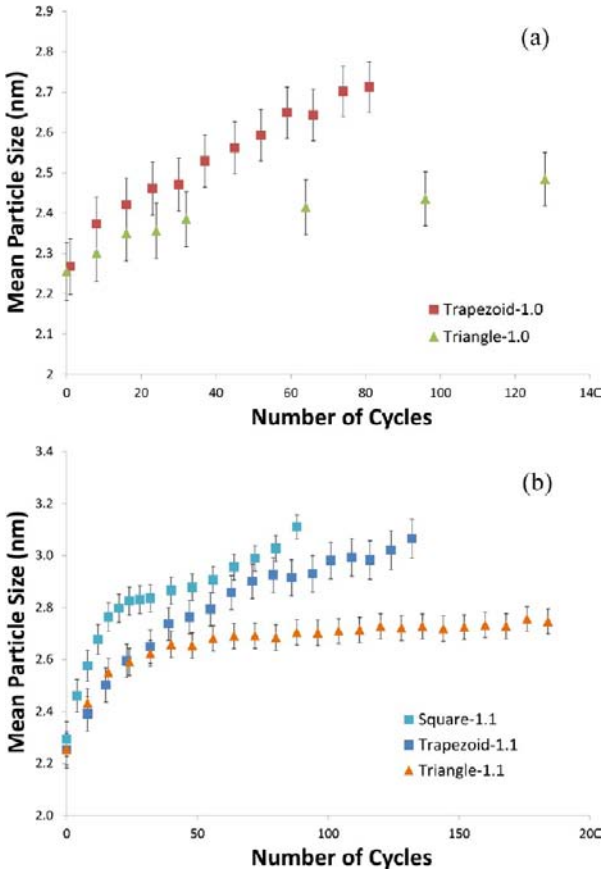

Figure 5. Mean particle size growth of Pt/C electrocatalysts as a function of the number of potential cycles with anodic potential limits of (a) 1.0 V and (b) 1.1 V.

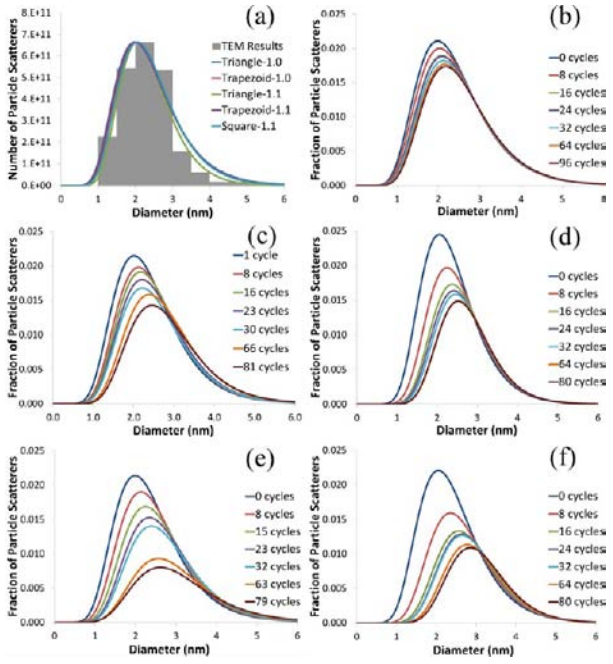

Figure 6. PSDs before cycling as compared to TEM of the (a) initial catalyst and evolution of PSDs over the duration of the experiments for (b) triangle-1.0, (c) trapezoid-1.0, (d) triangle-1.1, (e) trapezoid-1.1, and (f) square-1.1.

± 0.02 and 4.50 ± 0.02 nm diameter particles, respectively, is illustrated in Figure 7. The number of particles has been normalized to the initial number of particles at these diameters. These data show that all cycling profiles caused a loss of 1.5 nm particles, with the majority of this loss occurring within the first 30−60 cycles. An anodic potential limit of 1.1 V caused a faster rate of loss of these small particles than an anodic limit of 1.0 V. The greatest and most rapid loss of small particles resulted from the square-1.1 profile, which caused a loss of 90% of the 1.5 nm particles in just 24 cycles.

The increase in the number of larger particles was found to depend on the shape of the potential wave profile, as illustrated in Figure 7b for 4.5 nm diameter particles. The square and trapezoid wave profiles caused a significant increase in the number of larger particles, whereas the triangle wave profile showed very little or no increase. The contribution of each diameter in the PSD to the overall observed change in mean diameter can be calculated by comparing the number of particles at each diameter for the 0 and 80 cycle PSDs. Using this analysis and a bin size of 0.04 nm, it was found that loss of small particles (≤3 nm) accounts for 90% and 93% of the increase in the mean particles size for triangle-1.0 and triangle-1.1, respectively. This analysis also showed that the larger increase in mean particle diameter observed for the trapezoidal and square profiles, as compared to the triangle wave, is due to greater loss of small particles (≤3 nm), combined with a less significant contribution from an increase in the number of larger particles (>3 nm). This increase in the number of larger particles accounts for 12%, 25%, and 30% of the increase in mean particle size for square-1.1, trapezoid-1.1, and trapezoid-1.0, respectively. For the two triangle protocols, the change in mean particle diameter attributable to an increase in the number of larger particles is less than 10%.

To illustrate the effect of number of potential cycles on the number of particles at various diameters, Figure 8 shows a plot of the fraction of total Pt scatterers attributed to six different particle diameters (1.5−4.0 nm) as a function of number of square-1.1 cycles. This plot shows that initially, from the first cycle until the 48th cycle, particles of ∼3 nm in diameter are relatively stable. This stable diameter will be referred to as the "critical particle diameter", which is the diameter for which

dx.doi.org/10.1021/ja3038257 | J. Am. Chem. Soc. 2012, 134, 14823−14833

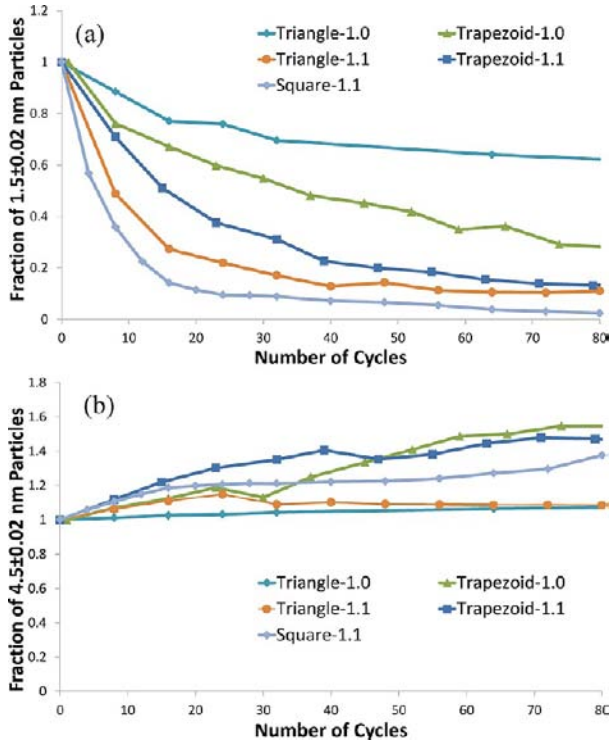

Figure 7. Plots of the fraction of (a) 1.5 nm and (b) 4.5 nm Pt particles remaining as a function of cycle number taken from the PSD for all five cycled experiments. The initial value is normalized to 1, representative of the initial number of particles at the given diameter.

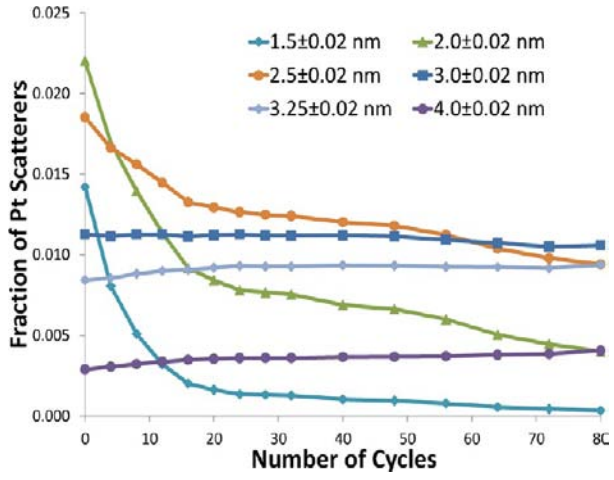

Figure 8. Plot of the fraction of Pt particle scatterers as a function of cycle number at periodic intervals taken from the PSD for the square-1.1 experiment.

there is an overall loss of particles smaller than this diameter and an overall increase in the number of particles larger than this diameter. After the 48th cycle this critical particle diameter shifts to ~3.25 nm. This initial critical particle diameter of ~3 nm is also seen in the triangle-1.0 and triangle-1.1 data, but the triangle cycling shows a slower shift of the critical particle diameter to a larger diameter than the square cycling. The trapezoid-1.0 and trapezoid-1.1 experiments show a much faster shift toward a larger critical particle diameter. This can be seen in the PSDs (Figure 6) by comparing the diameter where successive distributions intersect. The critical diameters after 80 cycles of the various cycling profiles are summarized in Table 3. These data illustrate that the critical particle diameter is dependent both on the upper potential limit and the potential profile: the rate of critical particle diameter increase is faster for 1.1 versus 1.0 V and decreases in the order trapezoid > square > triangle.

Geometric Surface Area. To determine the contribution of the various particle sizes to the initial overall surface area and the contribution of changes in the number of particles as a function of size to the surface area loss, geometric surface area (GSA) distributions were calculated on the basis of the number PSDs and the assumption of spherical particles. The average initial GSA, calculated from the five initial ASAXS-determined PSDs shown in Figure 7a, is 93 m^2/g. The average ECA measured for this catalyst, using the charge in the H_{upd} region of cyclic voltammograms, was found to be 58 m^2/g, resulting in an ECA to GSA ratio of 0.62. Holby et al., using TEM-determined PSDs to calculate GSA, found an ECA to GSA ratio of 0.63 for catalysts with mean particle diameter ranging from ~2−3 to 4−5 nm.[27] The constant GSA to ECA relationship over the particle sizes in this study implies that the GSA, as calculated from the ASAXS-determined PSDs, can be used to describe ECA losses with cycling.

The overall GSA losses after ~80 cycles of the five different potential profiles, as calculated from the initial and 80-cycle ASAXS-determined PSDs, are summarized in Table 3. The differences in the GSA losses for triangle-1.0 and triangle-1.1, 5% versus 21%, illustrate the detrimental effect of the higher upper potential limit of cycling on surface area loss, in agreement with accelerated rates of fuel cell cathode catalyst ECA loss with increasing anodic cycle limit.[7,8,23] For reference, Table 4 compares the ECA losses reported in the literature and the GSA losses determined in this study. This comparison illustrates the importance of temperature, type of electrolyte, environment, and operating conditions on ECA losses. Most notably, in the case of the MEA environment there is a "sink" for dissolved Pt (i.e., hydrogen crossing through the membrane that can reduce dissolved Pt in the membrane), which can increase Pt dissolution rates and ECA loss.[27,31] In addition, Dam et al. have shown that Pt dissolution rates and the

Table 3. Summary of Results of Potential Cycling Experiments and Oxide Coverage Calculations

				relative loss of Pt		oxide coverage	
experiment reference name	particle growth after 80 cycles (nm)	GSA loss after 80 cycles (%)	critical particle diameter (nm)	from electrode (ICP-MS)	particles < critical diameter	calcd	expl
triangle-1.0	0.18 ± 0.10	5	2.8	1.0	1.0	0.40	0.43 ± 0.06
trapezoid-1.0	0.44 ± 0.09	–	2.8	2.0	2.3	0.56	0.64 ± 0.11
triangle-1.1	0.43 ± 0.08	21	3.0	1.9	3.8	0.60	0.56 ± 0.10
trapezoid-1.1	0.68 ± 0.10	23	3.6	2.4	5.8	0.82	0.82 ± 0.08
square-1.1	0.73 ± 0.08	23	3.2	2.8	4.9	0.78	

dx.doi.org/10.1021/ja3038257 | J. Am. Chem. Soc. 2012, 134, 14823−14833

Table 4. Comparison of GSA Loss in This Study with ECA Losses Reported in the Literature

experimental condition	electrolyte	ECA loss (%)	temp (°C)	no. of cycles	potential limit (V) cathodic	potential limit (V) anodic	profile shape	sweep rate (mV/s)	cycle duration (s/cycle)	ref
aqueous	0.1 M $HClO_4$	5[a]	20	96	0.4	1.0	triangle	10	120	this study
aqueous	0.1 M $HClO_4$	21[a]	20	80	0.4	1.1	triangle	10	140	this study
aqueous	0.1 M $HClO_4$	3	20	500	0.5	1.0	triangle	50	20	Hasch et al.[62]
aqueous	0.5 M H_2SO_4	31	80	200	0.6	1.0	triangle	20	40	Holby et al.,[27] Sheng et al.[63]
aqueous	0.1 M $HClO_4$	16	60	100	0.6	1.0	square	–	6	Sugawara et al.[64]
aqueous	0.1 M $HClO_4$	15	20	7200	0.6	1.0	square	–	2	Takahashi and Kocha[32]
aqueous	0.5 M H_2SO_4	40	20	7200	0.6	1.0	square	–	2	Takahashi and Kocha[32]
aqueous	0.1 M $HClO_4$	37	20	60000	0.6	1.1	triangle	50	20	Wang et al.[65]
MEA	PFSA	14	80	100	0.1	1.0	triangle	50	36	Yasuda et al.[7]
MEA	PFSA	21	80	300	0.1	1.0	triangle	50	36	Borup et al.[8]

[a]GSA.

resulting ECA losses are strongly dependent on temperature, especially at >60 °C.[55,56]

The calculated initial GSA and GSA distributions after 96 and 80 cycles of triangle-1.0 and triangle-1.1 are shown in Figure 9 (a and b, respectively). Also included in these plots is the fraction of total surface area loss with cycling as a function of particle diameter range (0.2 nm bins). This comparison illustrates the effect of the anodic potential limit on the extent of loss of surface area arising from particles <3 nm in diameter. Figure 9 also illustrates the greater impact on change in ECA of loss of particles <3 nm than gain of particles >3 nm.

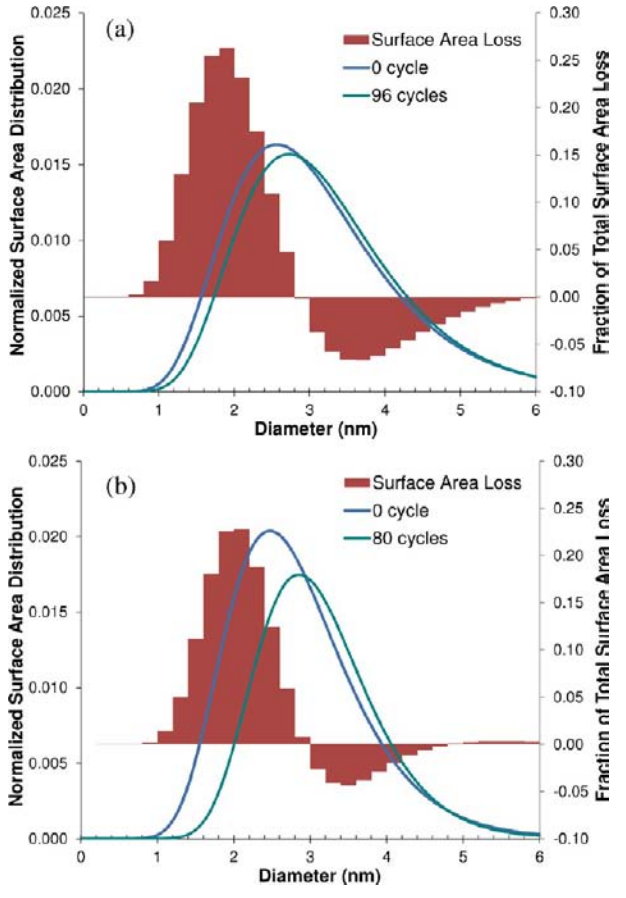

Figure 9. Geometric surface area distributions for the initial 0 cycles and after ~80 cycles for (a) triangle-1.0 and (b) triangle-1.1 (solid lines corresponding to the left-hand ordinate). Also included is the contribution of a given diameter range to the overall surface area loss after ~80 cycles (bar plot corresponding to the right-hand ordinate).

Concentration of Dissolved Pt. The ICP-MS-determined concentrations of dissolved Pt in the electrolyte after 160 cycles of the five potential protocols were 1.00, 2.01, 1.91, 2.40, and 2.80×10^{-8} M for triangle-1.0, trapezoid-1.0, triangle-1.1, traepzoid-1.1, and square-1.1, respectively. The fraction of the Pt lost from the electrode calculated from these concentrations ranged from 6.3×10^{-5} for triangle-1.0 to 1.8×10^{-4} for square-1.1. The dependence of Pt loss rate on cycling profile type, as determined from the ASAXS data, correlates very well with the dependence of loss rate on profile type seen in the ICP-MS data ($R^2 = 0.8$ for a plot of ASAXS loss rate vs ICP-MS loss rate). The absolute amounts of Pt loss from the electrode calculated from the ASAXS-derived PSDs were found to be larger than those determined using the ICP-MS data. The absolute loss of Pt as determined by these two techniques is discussed in the Supporting Information.

As shown in Figure 10a, the growth in the mean Pt particle size after 80 cycles, as determined from the ASAXS data (values in Table 3), shows a linear correlation ($R^2 = 0.96$) with the relative fraction of Pt lost from the electrodes after 160 cycles, as calculated using ICP-MS data. The ICP-MS-determined loss of Pt from the electrode for the various profiles, normalized to the loss observed for triangle-1.0, also correlates with loss of Pt with diameters less than the critical diameter, as determined from the ASAXS PSDs (Table 3, $R^2 = 0.75$). This correlation supports the conclusion that the main mechanism for growth in the mean particle diameter with potential cycling is preferential dissolution/loss of small Pt particles (<critical diameter of ~3 nm) into the electrolyte. The other possible mechanisms for Pt particle size growth, including both coarsening through redeposition and coalescence, would fail to show such a correlation, as they change particle size without changing in mass.

Oxide Coverage. Experimental and theoretical values for the oxide coverage reached during one cycle have been determined and are given in Table 3. The theoretical values were found to agree with the experimental values within the error of the experimental measurements, validating the model and supporting the validity of the calculated oxide coverage for square-1.1, which could not be determined experimentally.

dx.doi.org/10.1021/ja3038257 | J. Am. Chem. Soc. 2012, 134, 14823–14833

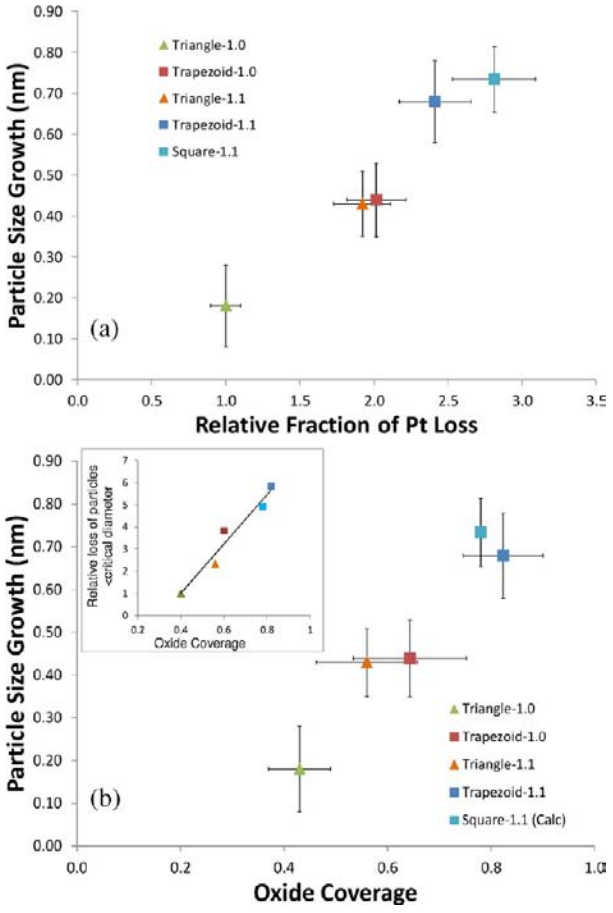

Figure 10. Growth of mean particle size after 80 cycles (ASAXS) as a function of (a) the relative fraction of dissolved Pt after 160 cycles (ICP-MS) for the five cycling experiments and (b) measured oxide coverage for four cycling experiments and the calculated oxide coverage for square-1.1. Inset: Fraction of Pt particles with diameters less than the critical diameter lost after 80 cycles, normalized to triangle-1.0.

For each of the five experiments, the particle size growth over the first 80 cycles is plotted as a function of the maximum oxide coverage reached during the cycle in Figure 10b. The largest growth in the mean particle size after 80 cycles was found for the trapezoid-1.1 and square-1.1 experiments, with values of 0.68 and 0.73 nm, respectively. These two experiments were also found to have the highest oxide coverage, with values of 0.82 and 0.78 monolayers, respectively. The triangle-1.0, showing the lowest oxide coverage of 0.40 monolayers, resulted in the least amount of growth, 0.31 nm.

Figure 10b suggests a monotonic relationship between the growth of the mean particle size and the maximum oxide coverage reached during one cycle for the considered potential ranges. The overall extent of Pt loss from the electrode, as determined by ICP-MS, and the extent of loss of Pt particles smaller than the critical diameter also show a monotonic relationship with the oxide coverage (Figure 10b inset and Table 3). This relationship among mean particle growth, Pt loss, and oxide coverage implies that formation of the oxide is playing a key role in the dissolution/coarsening process and in the resulting increase of the mean Pt nanoparticle diameter. This analysis therefore suggests that different extents of particle growth observed for different anodic potential limits and different potential profiles may all be controlled by the same underlying property, the peak oxide coverage reached during the potential cycle.

Mechanism of Particle Growth and ECA Loss. The ASAXS results indicate that the dominant mechanism of particle growth under the conditions of these experiments, an aqueous acid electrolyte and cycling up to relatively low anodic potentials, is preferential dissolution or loss of small particles. Other proposed growth processes, such as carbon corrosion and migration and coalescence of Pt particles on the carbon surface, would not show the observed correlation between particle growth, ECA loss, and dissolved Pt concentration. In addition, the higher of the two anodic limits used in this study, 1.1 V, has not been shown to cause major carbon corrosion, either in aqueous or fuel cell cycling tests.[57,58] For all potential cycling profiles used in this study, we observed a loss of the number of particles with diameters of <2.8−3.6 nm with cycling. This "critical particle diameter" was found to be a function of the upper potential limit of cycling and the potential profile. It can be speculated that the critical particle diameter of the electrocatalyst is specific to the initial PSD and the type of mechanism underlying the coarsening of the Pt nanoparticles. The initial dominant cause of change in mean particle diameter for all the profiles appears to be preferential dissolution or loss of small particles. The profiles with extended holds at the cathodic limit (trapezoid-1.0, trapezoid-1.1, and square-1.1) also have a minor contribution to mean particle growth of redeposition of dissolved Pt onto existing particles, which increases their diameter, as evidenced by an increase in the number of larger particles. This type of growth (i.e., dissolution/redeposition or electrochemical Ostwald ripening) is driven by the lower stability of the smaller particles and the corresponding greater driving force for dissolution. The identification of a critical size of approximately 3 nm beyond which Pt dissolution slows dramatically was also found in the theoretical work of Holby et al. for similar cycling conditions.[27]

This type of growth mechanism also helps explain the "plateau" region in the mean particle size growth of square-1.1 and trapezoid-1.1 seen in Figure 5b. The initial rapid increase in particle size for the profiles with an anodic limit of 1.1 V is primarily due to rapid dissolution of the smallest particles in the distribution with a minor contribution from redeposition as the Pt concentration in the electrolyte increases. The mean particle size then plateaus as these smallest and thermodynamically least stable particles diminish in number and the distribution is increasingly dominated by larger, more stable particles which are more difficult to dissolve. Beyond this plateau, further growth in mean particle size is then caused by a more evenly distributed dissolution/reprecipitation mechanism. The growth mechanism thus transitions from one dominated by dissolution to a dissolution/reprecipitation one as the system is potential cycled.

Pt dissolution, the dominant particle growth mechanism in this study, appears to be enhanced by or under control of the same factors as oxide formation and/or oxide reduction. Possible processes connecting the oxide formation/reduction and the Pt dissolution/reprecipitation are (1) formation and subsequent dissolution of the oxide layer, (2) oxide-induced enhancement of dissolution from metallic Pt sites, (3) dissolution during the oxide reduction process, or (4) formation of unstable Pt sites, as a result of oxide formation/reduction, which are then more prone to dissolution during the subsequent cycle.

dx.doi.org/10.1021/ja3038257 | J. Am. Chem. Soc. 2012, 134, 14823−14833

The previously demonstrated passivating properties of the Pt oxide suggest that process 1 is not likely. The presence of oxide formed during potentiostatic holds at >1.1 and >1.0 V has been shown to passivate polycrystalline Pt and Pt/C, respectively, against dissolution.[3,13,59] The lack of overall growth of the static-1.0 and static-1.1 experiments in this study reflect the low dissolution rates of Pt once passivated by oxide: nearly 24 h of potentiostatic conditions showed less than 0.1 nm of growth in the mean particle size. Therefore, these results point toward increased dissolution under cycling conditions occurring either as a result of, or concurrent with, the adsorption or desorption of the oxide layer or both (processes 2, 3, or 4).

If process 2 is dominant, then it might seem impossible to explain how potentiostatic formed oxide slows Pt dissolution while potential cycling induced oxide enhances Pt dissolution. However, this apparently contradictory behavior can perhaps be rationalized both by the slow formation of surface oxide and the slow evolution of the oxide layer from one that destabilizes Pt toward dissolution (present during cycling) to one that stabilizes and protects Pt against dissolution (present during constant potential holds). This change in the effect of the oxide may be due to restructuring of a destabilizing surface adsorbed oxygen layer to a two- or three-dimensional Pt oxide. Using in situ X-ray absorption spectroscopy, Imai et al. determined that at potentials above 1.0 V, oxide formation on Pt/C proceeds through surface adsorption of OH on atop sites, conversion of OH to O, followed by migration of O to 3-fold hollow sites, followed by place exchange of Pt and O to form a subsurface oxide and α-PtO_2-like oxide, followed by conversion of this α-oxide to β-PtO_2 at potentials above 1.2 V.[43] Correlating dissolution behavior with the oxide structures determined by Imai et al., it can be proposed that OH and O adsorbed on atop sites destabilize Pt toward dissolution, but the 3-fold hollow site O, the place-exchanged α-PtO_2-like oxide, and the β-PtO_2 stabilize surface Pt against dissolution. Using DFT, Ma and Balbuena calculated that surface absorbed O can shift the dissolution potential, which they explained as O stabilizing the Pt to which it is directly bound but destabilizing the Pt−Pt bond.[60]

In support of processes 3 and 4, it has also been speculated that the formation of and reduction of Pt oxide induces Pt ad-atoms and islands containing relatively low-coordinated, high-energy Pt surface sites.[22] These low-coordinated atoms may then be more prone to dissolution during the subsequent potential cycle (process 4) or could be removed during the oxide reduction (process 3).[13,22,61] Such a surface roughening process is consistent with the fact that Holby et al. found that modeling of Pt surface area loss required a dissolution rate during cycling that was about 500 times higher than during constant potential holds, although such a result could be consistent with process 2 as well.[52] The extent of roughening, or formation of unstable ad-atoms, can be expected to be proportional to the extent of oxidation, and thereby dissolution rates would increase with increasing extent of oxidation achieved during the anodic profile. Further work is required to establish the exact mechanism by which the oxide formation is enhancing the Pt dissolution.

CONCLUSIONS

The main conclusions from this study are as follows:

- Aqueous acid electrolyte experiments show that potentiostatic holds at 1.0 and 1.1 V result in minimal change in Pt nanoparticle mean diameter and surface area, whereas cycling up to these potentials results in significant particle growth and surface area loss.
- Pt particle growth and resulting surface area loss under potential cycling conditions are dominated by preferential dissolution/loss of small particles with a secondary particle growth mechanism of reprecipitation of the dissolved Pt onto existing particles.
- Experimental parameters such as anodic potential limit and the type of potential profile have a direct effect on the maximum oxide coverage per cycle.
- It is proposed that the oxide coverage reached during a cycle is playing a key role in the dissolution process and in the corresponding growth of the mean Pt nanoparticle size and loss of ECA. This understanding can reduce the complex changes in PSD and ECA resulting from various voltage profiles to the response to a single variable, oxide coverage.
- These results illustrate the importance of limiting oxide formation and reduction to extend the life of Pt-based PEFC cathode catalysts.
- ASAXS is a suitable technique for the in situ determination of the evolution of PSDs and geometric surface area distributions of Pt/C electrocatalysts with time and as a result of changing electrochemical conditions (e.g., potential cycling). This technique should also prove suitable for more complex systems (i.e., metal alloys, core−shell catalysts) and for studying Pt/C in operating PEFCs.

ASSOCIATED CONTENT

Supporting Information

Discussion on the absolute loss of Pt as determined by ASAXS and ICP-MS. This material is available free of charge via the Internet at http://pubs.acs.org.

AUTHOR INFORMATION

Corresponding Author

jagilbert@wisc.edu

Present Address

[§]Los Alamos National Laboratory, Los Alamos, NM 87545

Notes

The authors declare no competing financial interest.

ACKNOWLEDGMENTS

The authors thank the staff of Sector 12 at Advanced Photon Source, especially Soenke Seifert, for their knowledge and assistance during the ASAXS experiments. We also thank Jan Ilavsky for his discussions with regard to the ASAXS data analysis. We also acknowledge Yifen Tsai, Analytical Chemistry Laboratory, Argonne National Laboratory, for the ICP analyses. We thank the Department of Energy, Office of Energy Efficiency and Renewable Energy, Fuel Cell Technologies Program (Nancy Garland, DOE Program Manager), for funding this work, and the U.S. Department of Energy, Office of Basic Energy Sciences for support of the Advanced Photon Source and the Electron Microscopy Center. Argonne is a U.S. Department of Energy Office of Science Laboratory operated under Contract No. DE-AC02-06CH11357 by UChicago Argonne, LLC.

REFERENCES

(1) Costamagna, P.; Srinivasan, S. *J. Power Sources* **2001**, *102*, 242.
(2) Gasteiger, H. A.; Kocha, S. S.; Sompalli, B.; Wagner, F. T. *Appl. Catal., B* **2005**, *56*, 9.
(3) Ferreira, P.; la O', G.; Shao-Horn, Y.; Morgan, D.; Makharia, R.; Kocha, S.; Gasteiger, H. *J. Electrochem. Soc.* **2005**, *152*, A2256.
(4) de Bruijn, F. A.; Dam, V. A. T.; Janssen, G. J. M. *Fuel Cells* **2008**, *8*, 3.
(5) Xie, J.; Wood, D. L.; More, K. L.; Atanassov, P.; Borup, R. L. *J. Electrochem. Soc.* **2005**, *152*, A1011.
(6) Xie, J.; Wood, D. L.; Wayne, D. M.; Zawodzinski, T. A.; Atanassov, P.; Borup, R. L. *J. Electrochem. Soc.* **2005**, *152*, A104.
(7) Yasuda, K.; Taniguchi, A.; Akita, T.; Ioroi, T.; Siroma, Z. *Phys. Chem. Chem. Phys.* **2006**, *8*, 746.
(8) Borup, R. L.; Davey, J. R.; Garzon, F. H.; Wood, D. L.; Inbody, M. A. *J. Power Sources* **2006**, *163*, 76.
(9) Cleghorn, S. J. C.; Mayfield, D. K.; Moore, D. A.; Moore, J. C.; Rusch, G.; Sherman, T. W.; Sisofo, N. T.; Beuscher, U. *J. Power Sources* **2006**, *158*, 446.
(10) Schulze, M.; Schneider, A.; Gulzow, E. *J. Power Sources* **2004**, *127*, 213.
(11) Shi, Y.; Horky, A.; Polevaya, O.; Cross, J. In *Fuel Cell Seminar*; Palm Springs, CA, 2005.
(12) Borup, R.; Meyers, J.; Pivovar, B.; Kim, Y.; Mukundan, R.; Garland, N.; Myers, D.; Wilson, M.; Garzon, F.; Wood, D.; Zelenay, P.; More, K.; Stroh, K.; Zawodzinski, T.; Boncella, J.; McGrath, J.; Inaba, M.; Miyatake, K.; Hori, M.; Ota, K.; Ogumi, Z.; Miyata, S.; Nishikata, A.; Siroma, Z.; Uchimoto, Y.; Yasuda, K.; Kimijima, K.; Iwashita, N. *Chem. Rev.* **2007**, 3904.
(13) Shao-Horn, Y.; Sheng, W. C.; Chen, S.; Ferreira, P. J.; Holby, E. F.; Morgan, D. *Top. Catal.* **2007**, *46*, 285.
(14) Mathias, M.; Gasteiger, H.; Makharia, R.; Kocha, S.; Fuller, T.; Pisco, J. *Abstr. Pap. Am. Chem. Soc.* **2004**, *228*, U653.
(15) Akita, T.; Taniguchi, A.; Maekawa, J.; Sirorna, Z.; Tanaka, K.; Kohyama, M.; Yasuda, K. *J. Power Sources* **2006**, *159*, 461.
(16) Yasuda, K.; Taniguchi, A.; Akita, T.; Ioroi, T.; Siroma, Z. *J. Electrochem. Soc.* **2006**, *153*, A1599.
(17) Atrazhev, V.; Burlatsky, S.; Cipollini, N.; Condit, D.; Erikhman, N. *ECS Trans.* **2006**, *1*, 239.
(18) Patterson, T. *Topical Conference Proceedings of the AIChe Spring National Meeting*; New York, 2002.
(19) Shao-Horn, Y.; Ferreira, P.; Io, G. J.; Morgan, D.; Gasteiger, H.; Makharia, R. *ECS Trans.* **2006**, *1*, 185.
(20) Uchimura, M.; Kocha, S. *ECS Trans.* **2007**, *11*, 1215.
(21) Paik, C. H.; Saloka, G. S.; Graham, G. W. *Electrochem. Solid State Lett.* **2007**, *10*, B39.
(22) Uchimura, M.; Sugawara, S.; Suzuki, Y.; Zhang, J.; Kocha, S. S. *ECS Trans.* **2008**, *16*, 225.
(23) Yang, Z.; Ball, S.; Condit, D.; Gummalla, M. *J. Electrochem. Soc.* **2011**, *158*, B1439.
(24) Darling, R.; Meyers, J. *J. Electrochem. Soc.* **2003**, A1523.
(25) Darling, R.; Meyers, J. *J. Electrochem. Soc.* **2005**, A242.
(26) Garbarino, S.; Pereira, A.; Hamel, C.; Irissou, E.; Chaker, M.; Guay, D. *J. Phys. Chem. C* **2010**, *114*, 2980.
(27) Holby, E. F.; Sheng, W. C.; Shao-Horn, Y.; Morgan, D. *Energy Environ. Sci.* **2009**, *2*, 865.
(28) Kinoshita, K.; Lundquist, J. T.; Stonehart, P. *J. Electroanal. Chem. Interfacial Electrochem.* **1973**, *48*, 157.
(29) Rand, D. A. J.; Woods, R. *J. Electroanal. Chem.* **1972**, *35*, 209.
(30) Wang, X.; Myers, D.; Kariuki, N.; Kumar, R. In *Proceedings of the 211th ECS Meeting*; Chicago, Illinois, 2007; Vol. *701*.
(31) Myers, D.; Gilbert, J.; Wang, X.; Kariuki, N.; Niyogi, S.; Kropf, A. J.; Morgan, D.; Ball, S.; Sharman, J.; Theobald, B.; Hards, G. *Am. Chem. Soc., Div. Fuel Chem.* **2012**, *57*, 414.
(32) Takahashi, I.; Kocha, S. S. *J. Power Sources* **2010**, *195*, 6312.
(33) Smith, M. C.; Gilbert, J. A.; Mawdsley, J. R.; Seifert, S.; Myers, D. J. *J. Am. Chem. Soc.* **2008**, *130*, 8112.
(34) Haubold, H. G.; Wang, X. H.; Goerigk, G.; Schilling, W. *J. Appl. Crystallogr.* **1997**, *30*, 653.
(35) Brumberger, H. *Modern Aspects of Small-Angle Scattering*; Kluwer Academic Publishers: Dordrecht, 1995; Vol. *451*.
(36) Guinier, A.; Fournet, G. *Small-Angle Scattering of X-rays*; Wiley: New York, 1955.
(37) Materlik, G.; Sparks, C. J.; Fischer, K. *Resonant Anomalous X-ray Scattering, Theory and Applications*; Oxford: Elsiever Science: Amsterdam, NY, 1994.
(38) Vad, T.; Hajbolouri, F.; Haubold, H. G.; Scherer, G. G.; Wokaun, A. *J. Phys. Chem. B* **2004**, *108*, 12442.
(39) Narayanan, T. *Soft Matter: Scattering, Imaging, and Manipulation*, 1st ed.; Springer: Berlin, 2007.
(40) Coppola, R.; Giorgi, L.; Lapp, A.; Magnani, M. *Physica B* **2000**, *276*, 839.
(41) Haubold, H.; Wang, X.; Jungbluth, H.; Goerigk, G.; Schilling, W. *J. Mol. Struct.* **1996**, 283.
(42) Yu, C. F.; Holby, E. F.; Yang, R. Z.; Toney, M. F.; Morgan, D.; Strasser, P. *ChemCatChem* **2012**, *4*, 766.
(43) Imai, H.; Izumi, K.; Matsumoto, M.; Kubo, Y.; Kato, K.; Imai, Y. *J. Am. Chem. Soc.* **2009**, *131*, 6293.
(44) Teliska, M.; O'Grady, W. E.; Ramaker, D. E. *J. Phys. Chem. B* **2005**, *109*, 8076.
(45) Ilavsky, J.; Jemian, P. R. *J. Appl. Crystallogr.* **2009**, *42*, 347.
(46) Igor Pro 6, WaveMetrics, Inc.: Lake Oswego, OR.
(47) Stevens, D. A.; Zhang, S.; Chen, Z.; Dahn, J. R. *Carbon* **2003**, *41*, 2769.
(48) Borchert, H.; Shevehenko, E. V.; Robert, A.; Mekis, I.; Kornowski, A.; Grubel, G.; Weller, H. *Langmuir* **2005**, *21*, 1931.
(49) Vad, T.; Haubold, H. G.; Waldofner, N.; Bonnemann, H. *J. Appl. Crystallogr.* **2002**, *35*, 459.
(50) Tsao, C. S.; Chen, C. Y. *Physica B* **2004**, *353*, 217.
(51) Kim, S.; Meyers, J. P. *Electrochim. Acta* **2011**, *56*, 8387.
(52) Holby, E. F.; Morgan, D. *J. Electrochem. Soc.* **2012**, *159*, B578.
(53) Zehl, G.; Schmithals, G.; Hoell, A.; Haas, S.; Hartnig, C.; Dorbandt, I.; Bogdanoff, P.; Fiechter, S. *Angew. Chem., Int. Ed.* **2007**, *46*, 7311.
(54) Aragon, S. R.; Pecora, R. *J. Chem. Phys.* **1976**, *64*, 2395.
(55) Dam, V. A. T.; de Bruijn, F. A. *J. Electrochem. Soc.* **2007**, *154*, B494.
(56) Dam, V. A. T.; Jayasayee, K.; de Bruijn, F. A. *Fuel Cells* **2009**, *9*, 453.
(57) Makharia, R.; Kocha, S. S.; Yu, P. T.; Sweikart, M. A.; Gu, W.; Wagner, F. T.; Gasteiger, H. A. *ECS Trans.* **2006**, *1*, 3.
(58) Stevens, D. A.; Hicks, M. T.; Haugen, G. M.; Dahn, J. R. *J. Electrochem. Soc.* **2005**, *152*, A2309.
(59) Wang, X. P.; Kumar, R.; Myers, D. J. *Electrochem. Solid State Lett.* **2006**, *9*, A225.
(60) Ma, Y. G.; Balbuena, P. B. *J. Phys. Chem. C* **2008**, *112*, 14520.
(61) Jinnouchi, R.; Toyoda, E.; Hatanaka, T.; Morimoto, Y. *J. Phys. Chem. C* **2010**, *114*, 17557.
(62) Hasche, F.; Oezaslan, M.; Strasser, P. *ChemCatChem* **2011**, *3*, 1805.
(63) Sheng, W. C.; Chen, S.; Vescovo, E.; Shao-Horn, Y. *J. Electrochem. Soc.* **2012**, *159*, B96.
(64) Sugawara, S.; Ohma, A.; Tabuchi, Y.; Shinohara, K. *Int. Sci. J. Altern. Energy Ecol.* **2010**, *9*, 89.
(65) Wang, C.; van der Vliet, D.; More, K. L.; Zaluzec, N. J.; Peng, S.; Sun, S. H.; Daimon, H.; Wang, G. F.; Greeley, J.; Pearson, J.; Paulikas, A. P.; Karapetrov, G.; Strmcnik, D.; Markovic, N. M.; Stamenkovic, V. R. *Nano Lett* **2011**, *11*, 919.